INORGANIC CHEMISTRY FRONTIERS

RESEARCH ARTICLE

View Article Online
View Journal | View Issue

Cite this: *Inorg. Chem. Front.*, 2024, **11**, 5127

A D–A–D-type di-lophine derivative-based photoactive metal–organic framework: fluorescence sensing of UO_2^{2+} and photochromic behavior†

Yu-jian Cheng,[a] Zi-tong Chen,*[a] Hao-ran Ji,[a] Yuan Chen*[a] and Bao Li *[a,b]

Cadmium(II)-based metal–organic frameworks (MOFs) have been widely investigated for fluorescence sensing due to their chemical stability and tunable optical properties. However, how to precisely improve their selectivity and sensitivity to the target analytes is a key issue to be addressed. In this work, a photoactive MOF (PMOF) exhibiting specific cation fluorescence sensing and photochromism was constructed using Cd^{2+} and di-lophine based tetracarboxylic acid with D–A–D configuration. The effective combination of two components can form a stable porous framework with multiple electron transfer paths such as short-range electron transport in ligands and metal-to-ligand charge transfer (MLCT). The Cd-MOF exhibits strong absorption in the visible light range of 400–450 nm and strong fluorescence emission at 475 nm. Theoretical calculations show that the absorption and emission mainly originate from charge transfer between the metal and the ligand. In addition, due to the stable and anionic porous framework, the Cd-MOF demonstrated fluorescence quenching sensing to a variety of substrates, such as UO_2^{2+}, Fe^{3+}, $Cr_2O_7^{2-}$, MnO_4^-, nitrofuran antibiotics, TNP explosives, *etc*. In particular, the fluorescence detection constants (K_{sv}) of the Cd-MOF for UO_2^{2+} could reach 2.0×10^5 M^{-1}, which mainly originated from strong electrostatic interaction. The adsorption of UO_2^{2+} ions could effectively lower the energy level of the LUMO, which promotes the charge transfer from the $[Cd(COO)_4]^-$ node to UO_2^{2+} ions, leading to the fluorescence quenching of the Cd-MOF. In addition, the Cd-MOF can be photochromically responsive to visible light, generating a new strong absorption characteristic peak at 670 nm and a color change from yellow to green. The sensitive photochromic behavior should be assigned to the generation of imidazole radicals stabilized by the spatial confinement effect of the Cd-MOF, which lowers the energy level of $\pi^* \rightarrow \pi$ transition within the ligand. These findings suggest that the strategic synthesis of PMOFs utilizing D–A–D-type dilophine ligands can significantly modulate both the light absorption and fluorescence sensing capabilities, which paves a new way for the development of advanced, high-performance photoactive materials.

Received 4th May 2024,
Accepted 20th June 2024

DOI: 10.1039/d4qi01105h

rsc.li/frontiers-inorganic

Introduction

Nuclear energy is a desirable alternative due to its low emissions, high energy density, and established technology. While uranium, the primary element in nuclear power, offers these benefits, it also poses environmental and radioactive risks. The development of a more efficient and sensitive method for the detection of uranyl ions is critical for environmental protection, nuclear safety, and energy development.[1–5] Meanwhile, with the continuous development of science and industry, more and more environmental pollutants have been released, which has gradually attracted widespread attention. Environmental pollutants mainly include inorganic ions, toxic organic small molecules and so on. Since some of them play an indispensable role in many aspects, their trace detection is crucial.[6–12]

[a]*Key Laboratory of Material Chemistry for Energy Conversion and Storage, Semiconductor Chemistry Center, School of Chemistry and Chemical Engineering, Hubei Key Laboratory of Bioinorganic Chemistry & Materia Medica, Huazhong University of Science and Technology, Wuhan, Hubei, 430074, People's Republic of China. E-mail: chenzncu0514@163.com, chenyuan122800@163.com, libao@hust.edu.cn*

[b]*Jiangxi Provincial Key Laboratory of Functional Crystalline Materials Chemistry, Jiangxi University of Science and Technology, Ganzhou 341000, Jiangxi Province, P.R. China*

†Electronic supplementary information (ESI) available: Experimental sections, IR spectra and PXRD spectra. CCDC 2353038 (HUST-36). For ESI and crystallographic data on CIF or other electronic format see DOI: https://doi.org/10.1039/d4qi01105h

Photoactive metal–organic frameworks (PMOFs) are a new class of highly tunable and multifunctional materials that combine the optical activity of metal ions and the designability of organic ligands, showing potential for applications in photocatalysis, sensing and energy conversion. Currently, the research on PMOFs focuses on precisely controlling their structure and composition, achieving efficient absorption of visible and ultraviolet light to improve their solar energy utilization, stability and selectivity. Additionally, photochromic PMOFs have received less attention due to the difficulty in the selection of specific photo-responsive units for the framework, which would enhance the light absorption and charge separation efficiency.[8,13–18]

Similar to frequently-used photoactive groups such as azobenzenes, porphyrins, triphenylamines, and pyrenes, lophine possesses excellent photophysical and chemical properties and is capable of generating specific sensing properties in response to different external stimuli.[19–23] However, unlike the synthesis process of ligands containing the above conjugated units, the design and synthesis of lophine derivatives are relatively simple. For example, a variety of dilophine ligands with D–A–D configuration, which can effectively enhance the short-range transfer efficiency of photogenerated electrons by modulating the energy level structure of the central acceptor, have been developed. A series of MOFs with high efficiency in light energy utilization demonstrated the feasibility of their application as photocatalysts. However, the effectiveness of related research in the areas of fluorescence sensing and photochromic studies remains limited.[24–27]

Based on the above considerations, in this work, the integration of Cd^{2+} with d^{10} configuration and the di-lophine ligand successfully resulted in one anionic PMOF, [Cd(L)] (HUST-36, HUST = Huazhong University of Science and Technology), with sensitive fluorescence detection and photochromic properties. This anionic framework can effectively adsorb cations through electrostatic forces, increase host–guest interactions and alter electron transfer pathways to cause the optical sensing behaviour.[29–34] In agreement with expectations, the Cd-MOF has high sensitivity for the detection of UO_2^{2+} ions along with a fluorescence quenching constant of 2.0×10^5 M^{-1}, which is obviously higher than those of various other ions. In addition, thanks to its spatial confinement effect to stabilize imidazole radicals, the Cd-MOF can produce a sensitive response to visible light along with a color change from yellow to green. The synthesis, structural characterization, fluorescence sensing, and photochromic behavior of the Cd-MOF are discussed in detail below.

Experimental section

Experimental apparatus and reagents

All the reagents and solvents used during the experiments were purchased commercially and used without further purification. FT-IR spectra (4000–400 cm^{-1}) were obtained by using a VERTEX 70 Fourier transform mid-infrared (FT-MIR) spectrometer (KBr pressed slices). X-ray powder diffraction (XRD) was obtained using a SmartLab-SE X-ray diffractometer with a Cu-Kα target in the range of 5–50° at a scan rate of 10° min^{-1}. All fluorescence spectra were recorded using an RF-6000 fluorescence spectrophotometer. Ultraviolet–visible (UV-vis) absorption spectra were recorded at room temperature using a UV-3600 UV, visible and NIR spectrophotometer. Unpaired electrons of the samples were detected and the structural properties of their surroundings were explored with the EPR EMXmicro-6/1/P/L. The synthesis route of the di-lophine tetracarboxylic acid ligand (H_4L) is referred to in the literature.[21]

Synthesis of the Cd-MOF

$Cd(NO_3)_2{\cdot}4H_2O$ (10 mg) and H_4L (20 mg) were weighed in a 5 mL glass vial and then 3 mL of DMF was added and sonicated until well dispersed. Then, 0.5 mL of methanol was added and sonicated again, and then the mixture was placed in an oven at 120 °C for three days. At the end of the reaction, the vial was removed to a lower temperature to obtain golden yellow crystals. The solid was washed with DMF to remove unreacted ligands and metal ions, centrifuged, and dried in air to obtain pale yellow crystals in about 70% yield.

Fluorescence performance test

Considering the fluorescence properties of the Cd-MOF, we explored its detection potential as a fluorescence sensor in DMF solution.

(1) Detection of cations and anions. Firstly, different DMF solutions of cations and anions were prepared in volumetric flasks with a concentration of 5×10^{-3} mol L^{-1}. The cations included Al^{3+}, Ca^{2+}, Li^+, Zn^{2+}, K^+, Mg^{2+}, UO_2^{2+}, Fe^{3+}, Na^+, and Cd^{2+} and the anions included Cl^-, Br^-, I^-, NO_2^-, SCN^-, SO_4^{2-}, IO_3^-, CrO_4^{2-}, $Cr_2O_7^{2-}$, and MnO_4^-. A fully ground 3 mg sample was weighed and added to 2 mL of the solutions of different ions, sonicated and then tested for fluorescence at room temperature at a 360 nm excitation wavelength.

(2) Detection of antibiotics. Different antibiotic solutions were prepared in volumetric flasks, including sulfadiazine (SDZ), sulfamethoxazole (SMZ), sulfamethadiazole (SMT), thiamphenicol (TAP), enrofloxacin (ENR), norfloxacin (NOR), furazolidone (FZD), furazinonitrozole (NFZ), and tetracycline (TC), at a concentration of 5×10^{-3} mol L^{-1}. Then, 3 mg of the sample, which was weighed and fully ground, was added to 2 mL of solutions with different antibiotics, sonicated, and then tested for fluorescence at room temperature at an excitation wavelength of 360 nm.

(3) Detection of nitro-explosives. DMF solutions of nitro-explosives, including nitrobenzene (NB), 1,3-dinitrobenzene (1,3-DNB), 1,4-dinitrobenzene (1,4-DNB), 2,4-dinitrotoluene (2,4-DNT), 4-nitrophenol (4-NP), 2,4,6-trinitrotoluene (TNP), and 2,6-dinitrotoluene (2,6-DNT) were prepared in volumetric flasks with a concentration of 5×10^{-3} mol L^{-1} of nitro-explosive compounds. A fully ground 3 mg sample was weighed and added to 2 mL of a solution with different nitro explosives, sonicated, and then tested for fluorescence at an excitation wavelength of 360 nm at room temperature.

Photochromic test

Using a white CFL (compact fluorescent lamp) as the light source, the Cd-MOF and H_4L were irradiated for 1, 2, 3, 5, and 10 min and compared with the conditions of no light for 0 min to test the UV spectra, XRD spectra, and EPR spectra of the Cd-MOF and H_4L under various conditions, respectively.

Results and discussion

Structural description of the Cd-MOF

Single-crystal X-ray diffraction (SCXRD) analysis shows that the Cd-MOF crystallizes in the space group *C*2/*c* in a monoclinic crystal system (Table S1†). The asymmetric unit contains half a Cd^{2+} ion and half a ligand L^{4-} (Fig. 1a). Each Cd^{2+} ion is four-coordinated by four chelating carboxyl groups of different ligands to form a 4-connected $[Cd(COO)_4]^{2-}$ metal node. The bond length of Cd–O falls in the range of 2.244 to 2.454 Å (Table S2†), which is similar to those of other Cd(II) complexes. The carboxyl groups of each ligand coordinate with four Cd^{2+} ions in chelating mode to form an anionic 3D skeleton with high porosity and a typical $\{4^2{\cdot}8^4\}$ *PtS* topology. The high porosity facilitated the formation of a three-fold interpenetrating framework along with the reservation of 2D pores (Fig. 1). Along the *c*-axial direction, a large window with a size of 18.5049 × 8.3427 Å was presented. The pores were filled with solvent and counter ions such as $[(CH_3)_2NH_2]^+$ to balance the framework. Calculated using the PLATON program, the solvent accessible void space is about 45.4%. As shown in Fig. 2a, the powder XRD pattern is consistent with the simulated result from SCXRD, indicating the high purity of the synthesized sample. In the IR spectra, the characteristic peak of the carboxyl group in H_4L disappears in the Cd-MOF, indicating the successful coordination of the ligand to the metal ions (Fig. S1†).

From the SEM images of the Cd-MOF before and after the detection of UO_2^{2+}, it can be seen that the Cd-MOF exhibits a prismatic geometry, and its morphology does not change after

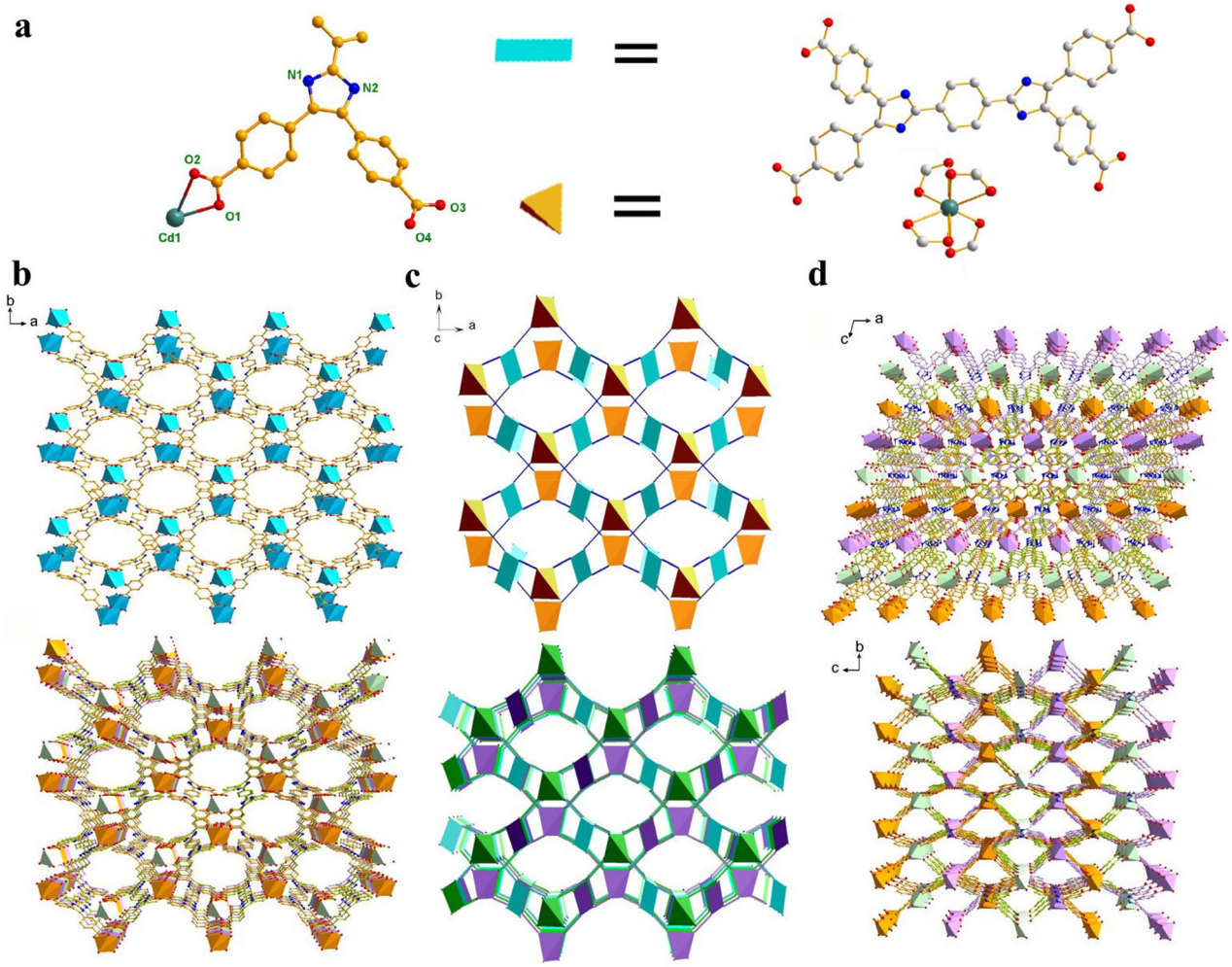

Fig. 1 (a) View of the asymmetric unit, (b) single and three-fold interpenetrating frameworks along the *c*-axial direction, (c) topologies of single and three-fold interpenetrating frameworks, (d) three-fold interpenetrating frameworks along the *a*-axis and the *b*-axis of the Cd-MOF (tetrahedra and rectangles represent metal clusters and di-lophine ligands, respectively).

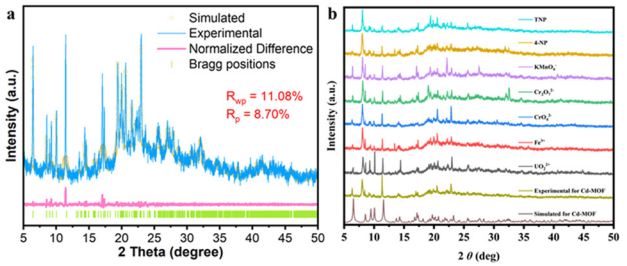

Fig. 2 (a) PXRD refinement of the synthesized Cd-MOF. (b) PXRD patterns of the Cd-MOF in aqueous solutions containing different guests.

the adsorption of UO_2^{2+} (Fig. S14 and S15†). From the EDS mapping images, it can be observed that the component elements are uniformly dispersed. The existence of uranium element in the Cd-MOF after detection was confirmed by EDS mapping, which verified the interaction between the Cd-MOF and UO_2^{2+}.

Solid-state fluorescence of the Cd-MOF

The solid-state fluorescence of the ligand and the Cd-MOF was tested under an excitation wavelength of 360 nm. As shown in Fig. 3a, the strongest emission peak of H_4L is near 537 nm, which may be caused by the $\pi^* \rightarrow \pi$ transition of the conjugated central ring. The characteristic emission peak of the Cd-MOF is 478 nm. The emission peak of the Cd-MOF is partially blue-shifted as compared to the free ligand, which may be assigned to metal-to-ligand charge transfer (MLCT).[35–37]

Theoretical calculations were carried out to further investigate the solid-state fluorescence emission mechanism of the ligand and the Cd-MOF. In order to reduce the computational workload, the main repeating unit of the Cd-MOF, which consists of one ligand and a Cd^{2+} ion, was selected, termed the Cd-unit. The overall structure was geometrically optimized, and the related optical properties of each model were calculated by TD-DFT (Fig. 3b–d). The related orbital levels and distribution are presented in Fig. 4.

The highest occupied molecular orbital (HOMO) and the lowest unoccupied molecular orbital (LUMO) of the Cd-unit were numbered as 205 and 206 orbitals, respectively. As shown in Fig. 4b, the HOMOs are mainly distributed around the metal clusters and partial ligands, while the LUMOs are mainly concentrated in the di-lophine rings of the ligands. The energy levels and orbital distributions of the HOMO−1 and LUMO+1 are similar to those of the HOMO and LUMO. Starting from the HOMO−2, the distribution becomes dis-

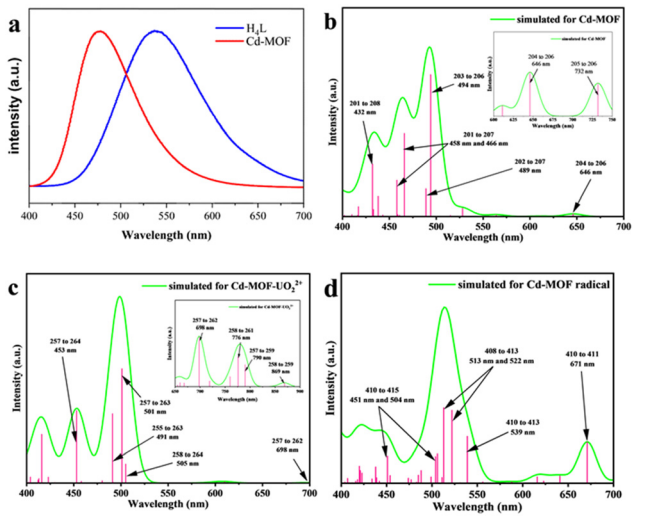

Fig. 3 (a) Fluorescence emission spectra of H_4L and the Cd-MOF. (b–d) Fluorescence emission spectra of the Cd-unit, the UO_2^{2+}@Cd-unit, and the Cd-unit-radical simulated by TD-DFT.

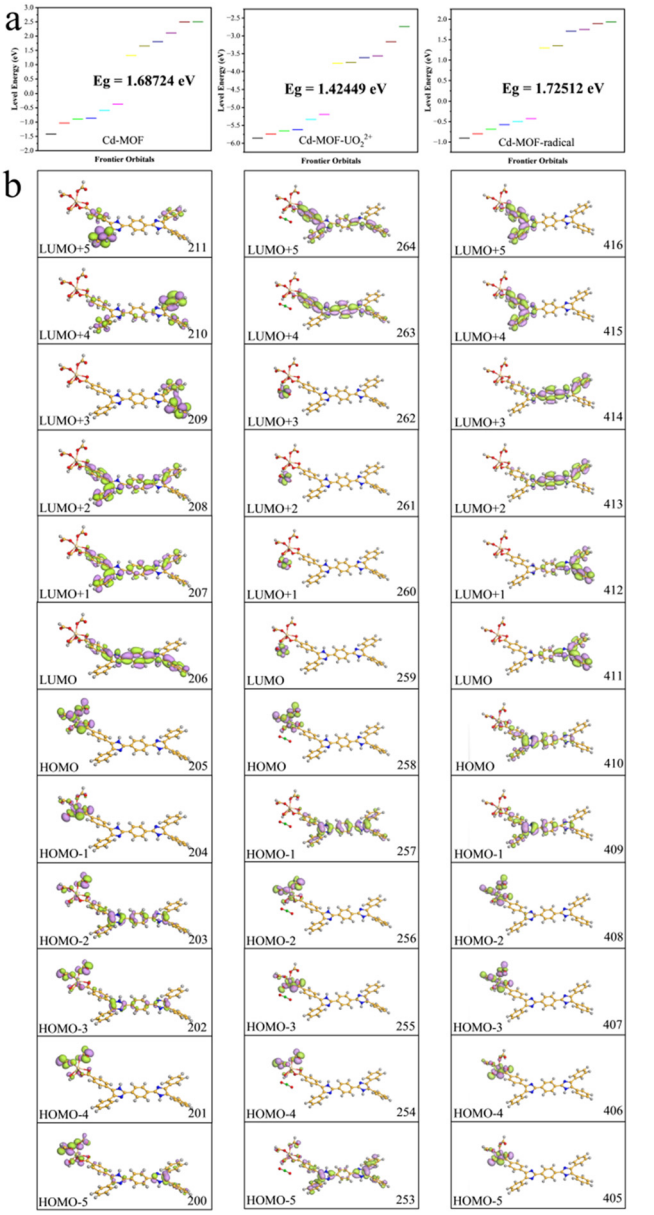

Fig. 4 Orbital energy levels (a) and distributions (b) of the Cd-unit, the UO_2^{2+}@Cd-unit, and the Cd-unit-radical.

persed over both the metal cluster and the ligand, suggesting that Cd^{2+} produces a better orbital overlap with the ligand, favoring MLCT behavior. Starting from the LUMO+2, the orbitals are still mainly concentrated on the whole ligand, but the distribution shifts from the central di-lophine rings to the adjacent benzene rings. Overall calculations show that the combination of cadmium ions and the tetracarboxylic acid ligand has effective orbital overlap, which lays a structural foundation for their application in photo-responsive applications.[28,38]

TD-DFT calculations show that the fluorescence spectra of the Cd-unit were consistent with the experimental results. The main simulated emission peaks are concentrated at 494, 466 and 432 nm (Fig. 3b). The peaks of 494, 466 and 432 nm correspond to the charge transfer among the 203↔206 orbital, the 201↔207 orbital, and the 201↔208 orbital. Observed from the distribution of orbitals, the simulated emission peaks at 466 and 432 nm are mainly attributed to MLCT, while the peak at 494 nm is mainly attributed to both the π–π* transition of the ligand and MLCT. The above results indicate that the introduction of heavy atoms partially sensitizes the di-lophine ligands, which effectively improves the energy transfer pathway within the MOF system and enhances the overall energy utilization.[28]

Luminescence detection of different cations

Considering the chemical stability and fluorescence properties of the Cd-MOF, its luminescence detection ability was further investigated. The sensing properties of various metal ions such as Al^{3+}, Ca^{2+}, Li^{+}, Zn^{2+}, K^{+}, Mg^{2+}, Na^{+}, Cd^{2+}, UO_2^{2+} and Fe^{3+} were tested for the first time. The fluorescence spectra of the Cd-MOF were tested at λ_{ex} = 360 nm after immersion in an aqueous solution containing different metal ions for 24 hours. Different metal cations showed significant effects on the Cd-MOF emission spectra (Fig. S3†). Al^{3+} had essentially no effect on the fluorescence emission intensity of the Cd-MOF. All other host–guest composite systems showed some degree of quenching effect. The quenching intensities, in descending order, were as follows: $Fe^{3+} > UO_2^{2+} > Mg^{2+} > Na^{+} > K^{+} > Ca^{2+} > Zn^{2+} > Li^{+} > Cd^{2+}$. The quenching efficiencies of Fe^{3+} and UO_2^{2+} on the Cd-MOF reached more than 95%. In addition, the high selectivity of the Cd-MOF for Fe^{3+} and UO_2^{2+} was explored by competition experiments testing coexisting metal cations at the same concentration (Fig. S7†). Competition experiments showed that the Cd-MOF exhibited high selectivity for Fe^{3+} and UO_2^{2+} even when interfered with by other cations. To evaluate the possibility of practical application of the Cd-MOF, detection of UO_2^{2+} in simulated seawater at different pH values was conducted. As shown in Fig. S16,† fluorescence quenching can still occur in simulated seawater at pH = 3, 7 and 11.

As shown in Fig. S17,† the fluorescence intensity of the solution gradually decreased as the ion concentrations of Fe^{3+} and UO_2^{2+} increased from 0 to 0.06 mM. The fluorescence quenching constants of the Cd-MOF in Fe^{3+} and UO_2^{2+} solutions can be obtained by using the Stern–Volmer equations.[39–41] In the concentration range of 0–4 μM, the S–V curves for UO_2^{2+} showed a good linear relationship with a fluorescence quenching constant K_{sv} value of 2.0×10^5 M^{-1}. In the concentration range of 0–60 μM, the S–V curves of Fe^{3+} showed a good linear relationship with a fluorescence quenching constant K_{sv} value of 1.7×10^4 M^{-1}. The correlation results showed that the Cd-MOF had strong interactions with Fe^{3+} and UO_2^{2+}, showing sensitive and selective recognition.

Fluorescence sensing mechanism

According to PXRD studies, the fluorescence detection of anions, nitro explosives and antibiotics by the Cd-MOF is not caused by structural transformations, since the diffraction is not significantly shifted from the peaks after immersion in solutions containing the corresponding analytes (Fig. 2b).

By comparing the UV-vis absorption spectra of various anions, cations, antibiotics and nitro explosives that can induce fluorescence quenching with the excitation spectra of the Cd-MOF (Fig. S2†), all the overlaps in the interval of 275–450 nm are to some extent in agreement with the quenching efficiency. Therefore, competitive absorption is the main reason for the fluorescence quenching response of the Cd-MOF to UO_2^{2+}, Fe^{3+}, $Cr_2O_7^{2-}$, MnO_4^{-}, nitrofuran antibiotics and TNP explosives. Given the fact that electrostatic repulsion exists between the anions and the anionic framework of the Cd-MOF, it is anticipated that the internal filtration effect (IFE) is also responsible for the fluorescence quenching.[42–44] It can be seen that the fluorescence intensities of most of the analytes before and after correction barely change, while IFE accounts for the cases of CrO_4^{2-} and TNP (Fig. S9†).

As mentioned above, the main fluorescence mechanism of the Cd-MOF is mainly due to the $\pi^* \rightarrow \pi$ transition and MLCT. Since appropriate host–guest interactions will ultimately regulate charge transfer between the metal node and the ligand, the fluorescence quenching mechanism of the Cd-MOF towards UO_2^{2+} ions has been theoretically investigated. Geometrical optimization of the theoretical models has been carried out. The analysis of the electrostatic potential (Fig. 5) of the optimized structure shows that the negatively charged centre of the Cd-unit is concentrated on the $[Cd(COO)_4]^{-}$ cluster, while the positively charged centre is concentrated on the hydrogen atom of the di-lophine center. After the introduction of UO_2^{2+} ions, the positive charge near the UO_2^{2+} ions and the negative charge near the metal clusters decrease, which may be due to the charge transfer from the metal clusters to the UO_2^{2+} ions, whereas the distribution of positive and negative charges on the ligands remains basically the same as that of the Cd-unit.

In addition, the introduction of UO_2^{2+} ions results in a reduction of the overall energy level gap and a shift of the LUMO from the ligand to the vicinity of the UO_2^{2+} ions. The HOMO, HOMO−2 and HOMO−4, on the other hand, are still concentrated in the metal node, whereas the HOMO−1 and HOMO−5 are distributed on the ligand. The energy levels and orbital distributions of the orbitals from the LUMO+1 to the LUMO+3 are similar to those of the LUMO, while the orbitals

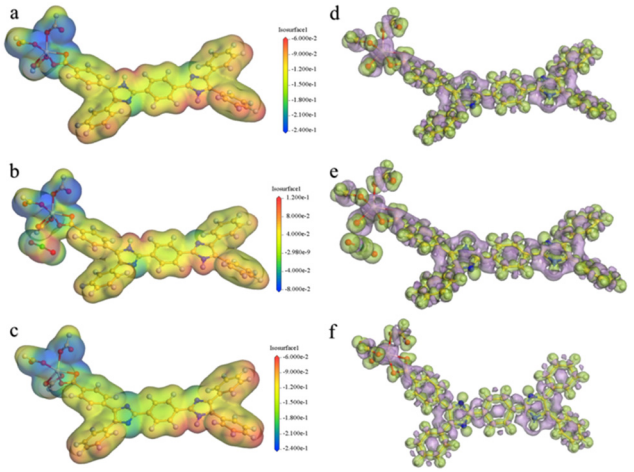

Fig. 5 Total (a–c) and deformation (d–f) electrostatic potentials for the Cd-unit, the UO_2^{2+}@Cd-unit and the Cd-unit-radical.

are mainly distributed on the ligand starting from the LUMO+4. Therefore, the introduction of UO_2^{2+} ions results in electron-deficient regions and lowers the orbital energy levels. The charge transfer from the Cd node to the UO_2^{2+} ions effectively quenches the original MLCT, resulting in the fluorescence quenching phenomenon. From the simulated spectra in Fig. 3c, it can be seen that the orbitals corresponding to the peaks at 453 nm and 501 nm are all concentrated on the ligand rather than on the MLCT of the Cd unit. The peaks at 698 nm and 790 nm are attributed to the charge transfer from the ligand to UO_2^{2+} and the peaks at 776 nm and 869 nm are assigned to the charge transfer from the metal cluster to UO_2^{2+}. The absence of the MLCT mechanism should be one of the reasons for the fluorescence quenching of the Cd-MOF.

Similar results can be obtained from the partial density of states (PDOS) of the Cd-unit and UO_2^{2+}@Cd-unit. As shown in Fig. 6, the Cd-unit has the largest proportion of p orbitals above the Fermi energy level, while after the adsorption of UO_2^{2+} ions, the percentages of p orbitals and d orbitals above the Fermi energy level are similar. The introduction of UO_2^{2+} effectively changes the distribution of the electron-deficient region and decreases the MLCT of the Cd-MOF. By analyzing the interaction of uranyl ions with the Cd-unit, it can be observed that the distance between the O atoms of UO_2^{2+} and Cd^{2+} and that of the C atoms on the carboxylate groups are 4.534, 5.499 Å and 4.043, 3.997 Å, respectively, implying electrostatic interaction and π–π interaction (Fig. S10†). Only three adsorption sites were found using the Monte Carlo method, all of which are in proximity to the metal nodes (Fig. 8a–c). The adsorption energy calculated for the three cases is almost the same, which is −103.162 kJ mol^{-1}. Similar results can be seen from the density field distribution images, as shown in Fig. 8d.

In order to confirm the correctness of the mononuclear metal node model, the periodic structure was also simulated. As shown in Fig. 7, the conduction band (CB) of the Cd-MOF is concentrated on the ligand, while the valence band (VB) is concentrated near the metal cluster. After the introduction of uranyl ions, the CB shifts to the uranyl ions. The differential electron density plot (Fig. S11†) shows that the electron density around Cd^{2+} before and after the introduction of UO_2^{2+} ions remains unchanged, illustrating the host–guest electro-

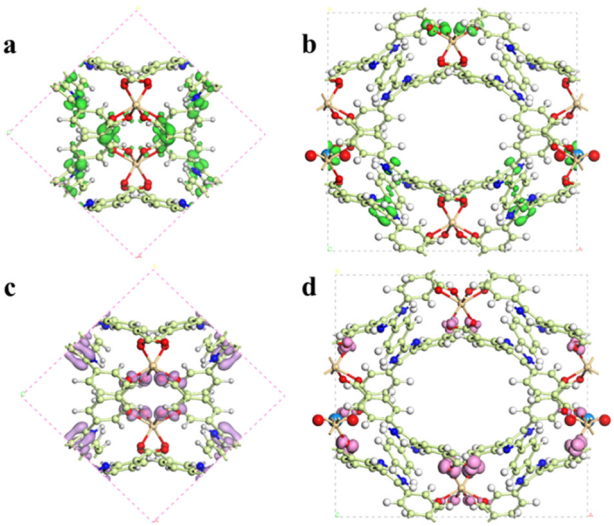

Fig. 7 CB and VB of the Cd-MOF (a and c) and the UO_2^{2+}@Cd-MOF (b and d).

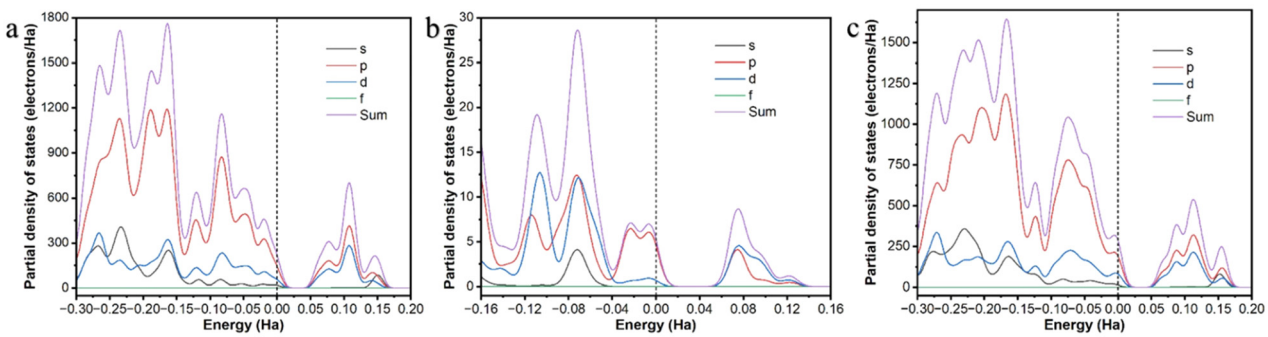

Fig. 6 (a–c) Partial density of the Cd-unit, the UO_2^{2+}@Cd-unit, and the Cd-unit-radical.

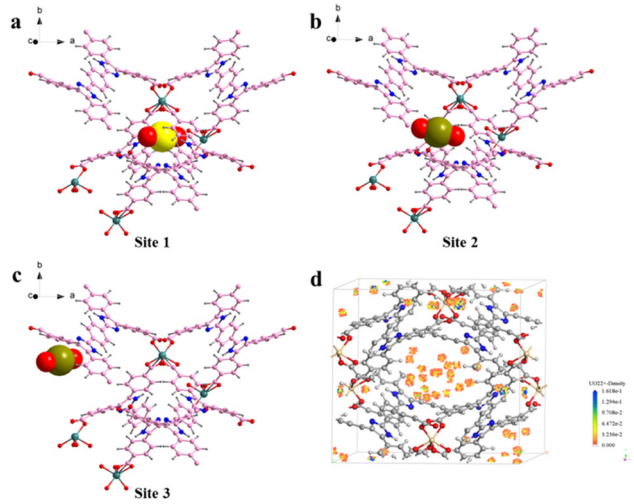

Fig. 8 (a–c) Three possible adsorption sites of UO_2^{2+} by the Cd-MOF by theoretical calculation; (d) the adsorption density field of UO_2^{2+} by the Cd-MOF.

static interactions. The band gap of the Cd-MOF is 2.273 eV (Fig. 9), which decreases to 1.106 eV after the introduction of UO_2^{2+}, illustrating an easier charge transfer from the Cd node to the guest ion. PDOS diagrams show that the Fermi energy level of the Cd-MOF is mainly related to the p-orbitals and d-orbitals, meaning the $[Cd(COO)_4]^-$ nodes. While above the Fermi energy level, the main components of p- and s-orbitals illustrate the location of the ligand. The related components clearly indicate the possibility of MLCT. After the introduction of UO_2^{2+}, the f orbitals also contribute to the orbitals above the Fermi energy level, revealing the feasibility of charge transfer from the metal node to UO_2^{2+}.

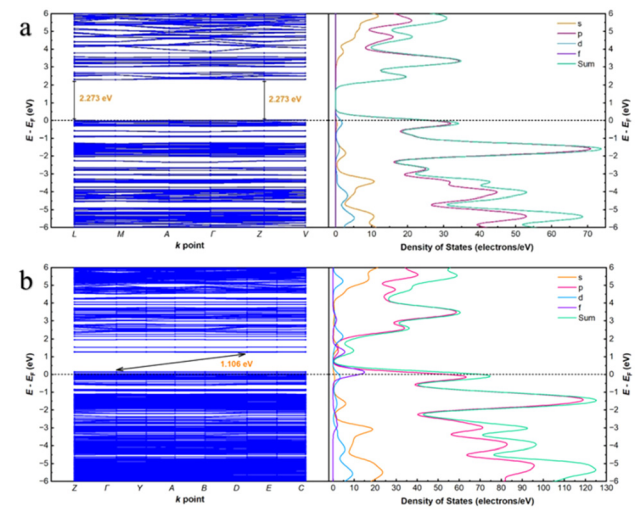

Fig. 9 Band structure *versus* PDOS of the Cd-MOF (a) and the UO_2^{2+}@Cd-MOF (b).

Photochromic behavior of the Cd-MOF

The unique photoactive motifs and periodic molecular arrays in the Cd-MOF ensure its potential application as an excellent photosensitizer. The photoactive behavior of the Cd-MOF was investigated using a white CFL (compact fluorescent lamp) as a light source.

After irradiation for 1 minute, the color of the Cd-MOF could change from yellow to green. The color of the Cd-MOF becomes greener as the exposure time increases (Fig. 10). The PXRD pattern of the Cd-MOF sample did not change with irradiation time (Fig. S12†), suggesting that the color change was not caused by the structural transformation.

UV-visible spectra of the fresh Cd-MOF show the main adsorption range of 200–420 nm, with the Tauc plot at 2.70 eV. In accordance with the color change, one new broad peak appeared at 678 nm under irradiation, and the intensity increased with the extension of irradiation time. After 10 min, the intensity and position of the peak no longer change. Under the same conditions, there was no significant change in pure H_4L. Therefore, the unique synergistic effects generated by the multicomponent combination are crucial for the sensitive photochromism of the Cd-MOF, such as the pre-designed photoactive motifs, the ordered stacking of molecular arrays, and the spatial confinement effect of the Cd-MOF.[45–52] The UV-visible absorption spectra of the fresh UO_2^{2+}@Cd-MOF show that the main absorption range is 200–420 nm, with a band gap of 2.68 eV (Fig. S16†). The minor difference in the color and band gap between the Cd-MOF and the UO_2^{2+}@Cd-MOF is due to the low loading rate of UO_2^{2+}. In spite of this, a trace of UO_2^{2+} has a significant influence on the fluorescence of the Cd-MOF.

Considering the presence of multiple nitrogen-containing sites, the generation of imidazolyl radicals by photogenerated electron transfer (PET) may be the main reason for the photochromic behavior of the Cd-MOF, which could be confirmed by the EPR results, as shown in Fig. 11. The radical signals were gradually enhanced with the increase in light exposure time until the intensity no longer changed at 10 min. In contrast, the radical signals of the ligands were almost unchanged under the same conditions, which is consistent with the results of UV-vis spectroscopy.

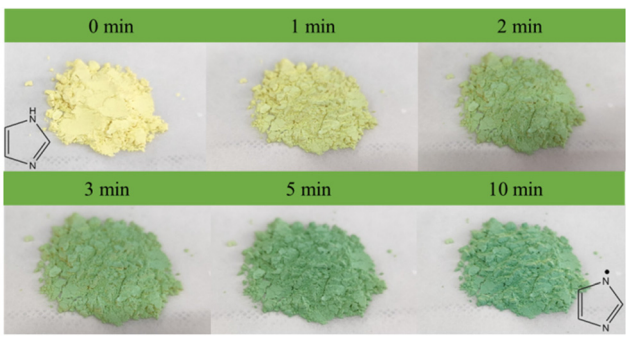

Fig. 10 Color change of the Cd-MOF with increasing irradiation time.

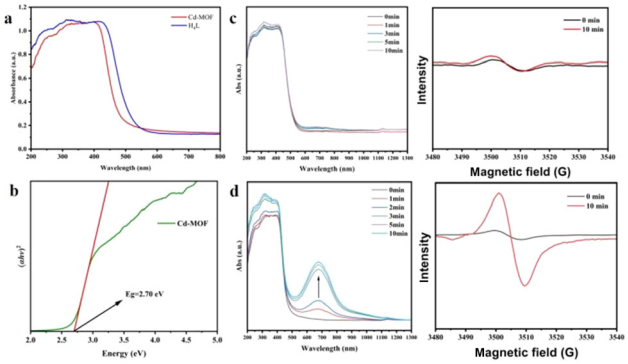

Fig. 11 (a and b) UV-visible diffuse reflectance spectra and the Tauc plot of the Cd-MOF; (c and d) UV-visible diffuse reflectance spectra and EPR spectra of H_4L and the Cd-MOF with irradiation time.

Compared to the theoretical calculations, a new strong peak at 671 nm occurs in the Cd-unit-radical, which matches well with the experimental results. The absorption peak here is attributed to the transition from the HOMO (410) to the LUMO (411) (Fig. 4b). The HOMO is mainly distributed around the metal nodes and partial ligands, while the proportion of the ligand increases, whereas the LUMO is still mainly concentrated near the bis-imidazole functional group. The energy levels and orbital distributions of the HOMO−1 and LUMO+1 of the Cd-unit-radical are similar to those of the Cd-unit. These results clearly indicate that the generation of free radicals may extend the scope of the HOMO and facilitate charge transfer from the metal node to the ligand, leading to a strong adsorption peak at 671 nm.

Conclusions

In summary, a photo-active MOF based on D–A–D-type dilophine tetracarboxylic acid has been successfully constructed with a Cd^{2+} node, which exhibits excellent fluorescence sensing of UO_2^{2+} and photochromic properties. The Cd-MOF exhibits a highly selective and sensitive fluorescence quenching response for a wide range of analytes, especially UO_2^{2+}, with a detection constant K_{sv} value of 2.0×10^5 M^{-1}, showing potential application in fluorescence sensing. The positive UO_2^{2+} ions exhibit strong electrostatic interaction with the anionic framework of the Cd-MOF and transfer the electron-deficient regions to the uranyl ions themselves, making charge transfer from the cadmium clusters to the uranyl ions more convenient, which in turn leads to fluorescence quenching of the MOF. In addition, due to the specific spatial confinement effect of the Cd-MOF to stabilize the photo-generated imidazole radical, photochromism can be observed under the irradiation of visible light, exhibiting a color change from yellow to green. These results indicate that the photosensitive properties of an MOF can be effectively regulated by the rational utilization of D–A–D-type dilophine tetracarboxylic acid ligands with suitable metal nodes, which opens up a new avenue for the development of high-performance photoactive materials.

Data availability

All relevant data are within the manuscript and its additional files.

Conflicts of interest

There are no conflicts to declare.

Acknowledgements

We gratefully acknowledge the National Natural Science Foundation of China (Grants 92161123 and 21971078), the Jiangxi Provincial Key Laboratory of Functional Crystalline Materials Chemistry (2024SSY05161), and the Open Project Program of Jiangxi Provincial Key Laboratory of Functional Molecular Materials Chemistry of Jiangxi University of Science and Technology (20212BCD42018) for financial support. We gratefully acknowledge the Analytical and Testing Center, Huazhong University of Science and Technology, for analysis and spectral measurements. We also thank the staff from the BL17B beamline of the National Center for Protein Sciences Shanghai (NCPSS) at the Shanghai Synchrotron Radiation Facility for their assistance during data collection.

References

1 Y. D. More, S. Mollick, S. Saurabh, S. Fajal, M. Tricarico, S. Dutta, M. M. Shirolkar, W. Mandal, J. C. Tan and S. K. Ghosh, Nanotrap Grafted Anionic MOF for Superior Uranium Extraction from Seawater, *Small*, 2023, **20**, 2302014.
2 R. G. Surbella, D. D. Reilly, M. A. Sinnwell, B. K. McNamara, L. E. Sweet, J. M. Schwantes and P. K. Thallapally, Multifunctional Two-Dimensional Metal–Organic Frameworks for Radionuclide Sequestration and Detection, *ACS Appl. Mater. Interfaces*, 2021, **13**, 45696–45707.
3 Y. Yuan, S. Feng, L. Feng, Q. Yu, T. Liu and N. Wang, A Bio–inspired Nano–pocket Spatial Structure for Targeting Uranyl Capture, *Angew. Chem., Int. Ed.*, 2020, **59**, 4262–4268.
4 N. Tang, J. Liang, C. Niu, H. Wang, Y. Luo, W. Xing, S. Ye, C. Liang, H. Guo, J. Guo, Y. Zhang and G. Zeng, Amidoxime-based materials for uranium recovery and removal, *J. Mater. Chem. A*, 2020, **8**, 7588–7625.
5 S. Zhang, H. Li and S. Wang, Construction of an Ion Pathway Boosts Uranium Extraction from Seawater, *Chem*, 2020, **6**, 1504–1505.

6 B. Wang, X.-L. Lv, D. Feng, L.-H. Xie, J. Zhang, M. Li, Y. Xie, J.-R. Li and H.-C. Zhou, Highly Stable Zr(IV)-Based Metal–Organic Frameworks for the Detection and Removal of Antibiotics and Organic Explosives in Water, *J. Am. Chem. Soc.*, 2016, **138**, 6204–6216.

7 P. Cen, C. Liang, L. Duan, M. Wang, D. Tian and X. Liu, A robust 3D In–MOF with an imidazole acid ligand as a fluorescent sensor for sensitive and selective detection of Fe^{3+} ions, *New J. Chem.*, 2020, **44**, 16076–16081.

8 Y. Wang, G.-P. Yang, P.-F. Zhang, L.-L. Ma, J.-M. Wang, G.-P. Li and Y.-Y. Wang, Microporous Cd(II) Metal–Organic Framework for CO_2 Catalysis, Luminescent Sensing, and Absorption of Methyl Green, *Cryst. Growth Des.*, 2021, **21**, 2734–2743.

9 S.-S. Chen, Z.-Y. Zhang, R.-B. Liao, Y. Zhao, C. Wang, R. Qiao and Z.-D. Liu, A Photoluminescent Cd(II) Coordination Polymer with Potential Active Sites Exhibiting Multiresponsive Fluorescence Sensing for Trace Amounts of NACs and Fe^{3+} and Al^{3+} Ions, *Inorg. Chem.*, 2021, **60**, 4945–4956.

10 H.-R. Fu, Y. Zhao, T. Xie, M.-L. Han, L.-F. Ma and S.-Q. Zang, Stable dye-encapsulated indium–organic framework as dual-emitting sensor for the detection of Hg^{2+}/$Cr_2O_7^{2-}$ and a wide range of nitro-compounds, *J. Mater.*, 2018, **6**, 6440–6448.

11 H. Zhang, J. Nai, L. Yu and X. W. Lou, Metal-Organic-Framework-Based Materials as Platforms for Renewable Energy and Environmental Applications, *Joule*, 2017, **1**, 77–107.

12 A.-G. Liu, X.-Y. Meng, Y. Chen, Z.-T. Chen, P.-D. Liu and B. Li, Introducing a Pyrazinoquinoxaline Derivative into a Metal–Organic Framework: Achieving Fluorescence-Enhanced Detection for Cs^+ and Enhancing Photocatalytic Activity, *ACS Appl. Mater. Interfaces*, 2023, **16**, 669–683.

13 M. J. Hurlock, M. F. Lare and Q. Zhang, Two Cd-Based Luminescent Coordination Polymers Constructed from a Truncated Linker, *Inorg. Chem.*, 2021, **60**, 2503–2513.

14 Q.-J. Jiang, J.-Y. Lin, Z.-J. Hu, V. K. S. Hsiao, M.-Y. Chung and J.-Y. Wu, Luminescent Zinc(II) Coordination Polymers of Bis(pyridin-4-yl)benzothiadiazole and Aromatic Polycarboxylates for Highly Selective Detection of Fe(III) and High-Valent Oxyanions, *Cryst. Growth Des.*, 2021, **21**, 2056–2067.

15 L. Zhu, B. Zhu, J. Luo and B. Liu, Design and Property Modulation of Metal–Organic Frameworks with Aggregation-Induced Emission, *ACS Mater. Lett.*, 2020, **3**, 77–89.

16 S. Wang, M. Gong, X. Han, D. Zhao, J. Liu, Y. Lu, C. Li and B. Chen, Embedding Red Emitters in the NbO-Type Metal–Organic Frameworks for Highly Sensitive Luminescence Thermometry over Tunable Temperature Range, *ACS Appl. Mater. Interfaces*, 2021, **13**, 11078–11088.

17 Y. Chen, A.-G. Liu, P.-D. Liu, Z.-T. Chen, S.-Y. Liu and B. Li, Enhancing energy transfer through visible-light-driven polymerization in a metal–organic framework, *J. Mater. Chem. A*, 2023, **11**, 18236–18246.

18 Y. Zhao, H. Zeng, X.-W. Zhu, W. Lu and D. Li, Metal–organic frameworks as photoluminescent biosensing platforms: mechanisms and applications, *Chem. Soc. Rev.*, 2021, **50**, 4484–4513.

19 J. Hu, T. Cheng, S. Dong, C. Zhou, X. Huang and L. Zhang, Multifunctional luminescent Cd(II)-based metal-organic framework material for highly selective and sensitive sensing 2,4,6-trinitrophenol (TNP) and Fe^{3+} cation, *Microporous Mesoporous Mater.*, 2018, **272**, 177–183.

20 X. Wang, Y. Zhang, Z. Shi, T. Lu, Q. Wang and B. Li, Multifunctional Zr-MOF Based on Bisimidazole Tetracarboxylic Acid for pH Sensing and Photoreduction of Cr(VI), *ACS Appl. Mater. Interfaces*, 2021, **13**, 54217–54226.

21 Y. Chen, A.-G. Liu, P.-D. Liu, Z.-Y. Zhang, F. Yu, W. Qi and B. Li, Application of Copper(II)–Organic Frameworks Bearing Dilophine Derivatives in Photocatalysis and Guest Separation, *Inorg. Chem.*, 2022, **61**, 16009–16019.

22 Y.-N. Zhou, L. Wang, J.-H. Yu, T.-Y. Ding, X. Zhang, C.-Q. Jiao, X. Li, Z.-G. Sun and Y.-Y. Zhu, Two Stable Cd-MOFs as Dual-Functional Materials with Luminescent Sensing of Antibiotics and Proton Conduction, *Inorg. Chem.*, 2022, **61**, 20111–20122.

23 C.-S. Liu, Z.-H. Zhang, M. Chen, H. Zhao, F.-H. Duan, D.-M. Chen, M.-H. Wang, S. Zhang and M. Du, Pore modulation of zirconium–organic frameworks for high-efficiency detection of trace proteins, *Chem. Commun.*, 2017, **53**, 3941–3944.

24 M. Y. Guo, G. Li, S. L. Yang, R. Bu, X. Q. Piao and E. Q. Gao, Metal–Organic Frameworks with Novel Catenane–like Interlocking: Metal–Determined Photoresponse and Uranyl Sensing, *Chem. – Eur. J.*, 2021, **27**, 16415–16421.

25 S. Zhang, K. Zhang, S. Du, S. Chen, Q. Zhang, X. Shi, Q. Meng, Y. Gai and K. Xiong, A viologen-based Cd(ii) coordination polymer as a multifunctional platform for photochromism, chemochromism and a broad range of fluorescence pH sensing, *Dalton Trans.*, 2023, **52**, 11773–11779.

26 H.-Y. Li, Y.-L. Wei, X.-Y. Dong, S.-Q. Zang and T. C. W. Mak, Novel Tb-MOF Embedded with Viologen Species for Multi-Photofunctionality: Photochromism, Photomodulated Fluorescence, and Luminescent pH Sensing, *Chem. Mater.*, 2015, **27**, 1327–1331.

27 Z.-H. Guo, P.-F. Zhang, L.-L. Ma, Y.-X. Deng, G.-P. Yang and Y.-Y. Wang, Lanthanide–Organic Frameworks with Uncoordinated Lewis Base Sites: Tunable Luminescence, Antibiotic Detection, and Anticounterfeiting, *Inorg. Chem.*, 2022, **61**, 6101–6109.

28 Z. G. Gu, D. J. Li, C. Zheng, Y. Kang, C. Wöll and J. Zhang, MOF–Templated Synthesis of Ultrasmall Photoluminescent Carbon–Nanodot Arrays for Optical Applications, *Angew. Chem., Int. Ed.*, 2017, **56**, 6853–6858.

29 S. Li, B. Wang, G. Liu, X. Li, C. Sun, Z. Zhang and X. Wang, Achieving ultra-trace analysis and multi-light driven photodegradation toward phenolic derivatives via a bifunctional catalyst derived from a Cu(i)-complex-modified polyoxometalate, *Inorg. Chem. Front.*, 2024, **11**, 1561–1572.

30 Y.-L. Wang, X.-Y. Li, S.-D. Han, J. Pan and Z.-Z. Xue, A Cu_2I_2-Based Coordination Framework as the Selective Sensor for Ag^+ and the Effective Adsorbent for I_2, *Cryst. Growth Des.*, 2022, **22**, 3719–3726.
31 Z.-Z. Xue, Y.-L. Wang, Y. Zhang, G.-Y. Fan, S.-D. Han and J. Pan, Construction of Cu(I)-Organic Frameworks with Effective Sorption Behavior for Iodine and Congo Red, *Inorg. Chem.*, 2022, **61**, 14148–14155.
32 X. Zhou, Y. Li, X. Li, S. Du, Y. Yang, K. Xiong, Y. Xie, X. Shi and Y. Gai, A Multifunctional Coordination Polymer Constructed by Viologen Derivatives: Photochromism, Chemochromism, and MnO_4^- Sensing, *Inorg. Chem.*, 2022, **61**, 11687–11694.
33 J. Zhang, L. Chen, Q. Chen, Y. Yue, Q. Chen, D. Yin and C. Zhang, An efficient dual-response luminescent metal-organic framework sensor constructed by new photochromic ligand, *Dyes Pigm.*, 2023, **220**, 111751.
34 P. Li, M.-Y. Guo, L.-L. Gao, X.-M. Yin, S.-L. Yang, R. Bu and E.-Q. Gao, Photoresponsivity and antibiotic sensing properties of an entangled tris(pyridinium)-based metal–organic framework, *Dalton Trans.*, 2020, **49**, 7488–7495.
35 B. Wu, T. Sun, N. Liu, L. Lu, R. Zhang, W. Shi and P. Cheng, Modulation of Z-Scheme Heterojunction Interface between Ultrathin C_3N_5 Nanosheets and Metal–Organic Framework for Boosting Photocatalysis, *ACS Appl. Mater. Interfaces*, 2022, **14**, 26742–26751.
36 D. H. Liu, K. Nagashima, H. Liang, X. L. Yue, Y. P. Chu, S. Chen and J. Ma, Chemoselective Quinoline and Isoquinoline Reduction by Energy Transfer Catalysis Enabled Hydrogen Atom Transfer, *Angew. Chem., Int. Ed.*, 2023, **62**, e202312203.
37 B. Wu, N. Liu, L. Lu, R. Zhang, R. Zhang, W. Shi and P. Cheng, A MOF-derived hierarchical CoP@$ZnIn_2S_4$ photocatalyst for visible light-driven hydrogen evolution, *Chem. Commun.*, 2022, **58**, 6622–6625.
38 L. Zhang, X.-L. Li, D. Luo, P. Xiao, W. Xiao, Y. Song, Q. Ang and B. Liu, Strategies to Achieve High-Performance White Organic Light-Emitting Diodes, *Materials*, 2017, **10**, 1378–1435.
39 S. Xian, H.-L. Chen, W.-L. Feng, X.-Z. Yang, Y.-Q. Wang and B.-X. Li, Eu(III) doped zinc metal organic framework material and its sensing detection for nitrobenzene, *J. Solid State Chem.*, 2019, **280**, 47–52.
40 J.-K. Chen, S.-M. Yang, B.-H. Li, C.-H. Lin and S. Lee, Fluorescence Quenching Investigation of Methyl Red Adsorption on Aluminum-Based Metal–Organic Frameworks, *Langmuir*, 2018, **34**, 1441–1446.
41 L.-L. Xu, Q.-F. Zhang, D. Wang, G.-W. Wu and H. Cai, Construction of a Luminescent Cadmium-Based Metal–Organic Framework for Highly Selective Discrimination of Ferric Ions, *Molecules*, 2021, **26**, 6847–6857.
42 S. Chen, Y. L. Yu and J. H. Wang, Inner filter effect-based fluorescent sensing systems: A review, *Anal. Chim. Acta*, 2018, **999**, 13–26.
43 S. A. Diamantis, A. Margariti, A. D. Pournara, G. S. Papaefstathiou, M. J. Manos and T. Lazarides, Luminescent metal–organic frameworks as chemical sensors: common pitfalls and proposed best practices, *Inorg. Chem. Front.*, 2018, **5**, 1493–1511.
44 T. Weitner, T. Friganovic and D. Sakic, Inner Filter Effect Correction for Fluorescence Measurements in Microplates Using Variable Vertical Axis Focus, *Anal. Chem.*, 2022, **94**, 7107–7114.
45 A. Omrani, Z. Deliballi, K. Kaya, B. Kiskan and M. Akgun, Catalytic Role of Nanoconfinement inside MIL-125 (Ti) on the Ring-Opening Polymerization of Simple Benzoxazines, *ACS Appl. Polym. Mater.*, 2023, **6**, 253–264.
46 C. J. Setter, M. B. Price, L. Conte, W. Schmitt, S. R. Batten, C. Richardson, M. R. Hill, R. Babarao and L. K. Macreadie, Mixed donor, phenanthroline photoactive MOFs with favourable CO_2 selectivity, *Chem. Commun.*, 2020, **56**, 13377–13380.
47 J. Li, S. Yuan, J. S. Qin, J. Pang, P. Zhang, Y. Zhang, Y. Huang, H. F. Drake, W. R. Liu and H. C. Zhou, Stepwise Assembly of Turn–on Fluorescence Sensors in Multicomponent Metal–Organic Frameworks for in Vitro Cyanide Detection, *Angew. Chem., Int. Ed.*, 2020, **59**, 9319–9323.
48 Z.-Z. Xue, Y.-L. Wang, J. Yang, H.-F. Sun and J. Pan, Water-Stable Cd(II)-Based Metal–Organic Framework: Antibiotic Detection and Photochromism Behavior, *Cryst. Growth Des.*, 2023, **23**, 6960–6966.
49 Z.-G. Liang, G.-M. Li, X.-Y. Ren, J.-H. Li, J. Pan and S.-D. Han, Photochromic Supramolecular Isomers Derived from Pb(II)-Bipyridinedicarboxylate Complexes, *Inorg. Chem.*, 2023, **62**, 8663–8669.
50 Z.-Z. Xue, Y.-L. Wang, J. Yang, H.-F. Sun and J. Pan, Water-Stable Cd(II)-Based Metal–Organic Framework: Antibiotic Detection and Photochromism Behavior, *Cryst. Growth Des.*, 2023, **23**, 6960–6966.
51 S. Li, J. Sun, G. Liu, S. Zhang, Z. Zhang and X. Wang, A new Keggin-type polyoxometallate-based bifunctional catalyst for trace detection and pH-universal photodegradation of phenol, *Chin. Chem. Lett.*, 2024, **35**, 109148.
52 S. Li, B. Wang, G. Liu, X. Li, C. Sun, Z. Zhang and X. Wang, Achieving ultra-trace analysis and multi-light driven photodegradation toward phenolic derivatives via a bifunctional catalyst derived from a Cu(I)-complex-modified polyoxometalate, *Inorg. Chem. Front.*, 2024, **11**, 1561–1572.